ELSEVIER

Chemical Engineering Journal 72 (1999) 1–17

Chemical Engineering Journal

Rotating membrane disk filters: design evaluation using computational fluid dynamics

Christophe A. Serra[a], Mark R. Wiesner[a,*], Jean-Michel Laîné[b]

[a] *Department of Environmental Science and Engineering, Rice University, 6100 Main Street, Houston, TX 77005, USA*

[b] *CIRSEE, Suez – Lyonnaise des Eaux, Le Pecq, France*

Received 8 January 1998; accepted 29 July 1998

Abstract

Computational fluid dynamics is used to investigate designs for rotating membrane disk filters. Simulations have been run for the case of water permeating through a membrane disk rotating in a pressurized housing. The water was assumed to be Newtonian, incompressible, non-fouling and isothermal. A κ–ε model was used to describe turbulent flow in the vessel surrounding the rotating disk. Similar to a non-porous disk, the rotation of the membrane disk induces a recirculating flow pattern of the fluid within the vessel. However, the centrifugal force acting on the permeate may locally increase the permeate side pressure above the feed side pressure resulting in a negative local transmembrane pressure. Hence, a portion of the membrane is subject to a reversed flow of permeate which reduces effectiveness of membrane area and may damage the membrane. This 'back pressure' phenomenon can be avoided by a careful choice of the operating conditions and design parameters. The propensity for 'back pressure' is higher when the membrane is more permeable but can be reduced by increasing the feed flow rate or decreasing the disk diameter (i.e. the membrane area).

Keywords: Membrane; Computational fluid dynamics; Rotating disk; Turbulent flow; Filter design

1. Introduction

The use of membrane filtration technologies in liquid–solid and emulsion separations has proliferated over the last two decades. These technologies are widely used by many industries to produce potable water, treat domestic wastewater, purify industrial wastewater, prepare waters for boil feed or cooling, and reduce the volume of hazardous waste as well as many other applications [1,2]. However, the accumulation of materials near the membrane–liquid interface and the resultant permeate flux decline or increase in transmembrane pressure known as fouling, remain an obstacle to a more extensive application of these membrane processes. Increasing the shear stress at the membrane surface to reduce particle deposition is often used to limit fouling.

In the classical cross-flow filtration, the shear stress at the membrane surface is increased by applying a tangential flow. Therefore, the shear stress and the feed flow rate are linked. A higher shear stress implies a higher flow rate and subsequently higher energy expenditure due to the pressure drop and sometimes the need to recycle flow. In rotating filters, the shear stress is independent of the flow rate since it relies on the speed of membrane rotation.

One consequence of the movement of the membrane rather than the fluid to create shear stress is the potential for treating very high concentrated suspensions usually considered as 'unfilterable'. Rotating filters have been applied in clarification [3–5] and for the concentration of biological products [6–9]. Recent studies showed that these filtration devices can be successfully used to treat power activated carbon feed suspensions as highly as 200 g l^{-1} [10,11].

Rotating membrane filters can be implemented by rotating either the membrane or a baffle near the membrane [12] and are commonly one of two types: rotating cylinders or rotating disks. The former referred as annular membranes consist of two concentric cylinders separated by a small gap and takes advantage of Taylor vortices when one of those cylinders is rotating. The latter consist of two axial disks and takes advantage of a radial flow in the vicinity of the rotating disk to reduce particles deposition on the membrane as well as the centrifugal force and shear stress exerting on particles deposited on the membrane surface to drive them back into the bulk fluid.

*Corresponding author. Tel.: +1-713-285-5129; fax: +1-713-285-5203; e-mail: wiesner@ruf.rice.edu

1385-8947/99/$ – see front matter
PII: S1385-8947(98)00128-4

Although rotating cylinder filters have been extensively studied [3,5,6,13–21], few attempts have been made to systematically evaluate designs for rotating disk filters despite the fact that several studies on slurries clarification and biological products concentration have been reported [4,9,22–26]. However, the fundamental fluid mechanics of non-porous rotating disks has been investigated in great detail [27–33]. Early characterization of the hydrodynamics of a rotating disk in an enclosed vessel was reported by Daily and Nece in 1960 [28]. They showed that the hydrodynamics of the system are governed by the Reynolds number ($\mathrm{Re} = \omega R^2/\nu$) and the axial clearance (s/R) where ω is the rotational speed, R the disk radius, ν the fluid kinematic viscosity, and s the gap between the disk and a stationary wall. By measuring the torque acting on the shaft and correlating the frictional torque coefficient with the Reynolds number and axial clearance, they were able to differentiate four flow regimes. For laminar flow ($\mathrm{Re} < 10^5$) and small clearance, the boundary layers on the disk and end-wall are merged, so the velocity varies continuously across the gap 's' (regime I). As the clearance increases, the boundary layers separate themselves and the bulk fluid rotates with an angular velocity less than ω, so the velocity is expected to be constant (regime II). For turbulent flow ($\mathrm{Re} > 3 \times 10^5$), two other similar regimes can be found depending on the magnitude of the clearance (regime III and IV). Recently, Rudniak and Wronski [33] used numerical simulations to characterize laminar flow hydrodynamics in an enclosed rotating disk filter. They showed that the fluid in the vicinity of the rotating disk moves radially to the disk tip, is then thrown away by centrifugal forces and returns axially along the vessel wall until it encounters the end-wall at separation distance 's' where it returns in a radial direction toward the shaft. By comparison with the case of non-porous disks, very little work has been done on the fluid mechanics of membrane disk systems, particularly as they affect membrane performance and the potential for reducing fouling.

In this work, we consider the fluid mechanics of a rotating membrane disk filter as a function of critical elements of system design. Computational fluid dynamics (CFD) is used to investigate the effect of system geometry and operating conditions on membrane performance. We might anticipate that there are many similarities in the mechanics of bulk fluid motion for porous and non-porous disks. However, in the following sections we show that rotation produce an important effect on the net permeability of the membrane disk.

2. Methodology

2.1. Filtration unit

The filtration unit consists of a single disk with dimensions equal to those of a laboratory unit (Fig. 1) to facilitate comparison of computational results with earlier experimental evaluations [10,11]. The membrane disk is mounted on a hollow rotating shaft via two retaining sleeves and washers (Fig. 2). The disk itself is assumed to be a porous medium with a membrane surface on each of its faces and a retaining seal at the disk tip. The feed inlet is assumed to be a slit around the vessel opposite the tip of the membrane disk. Permeate exits through the hollow-shaft (Fig. 1). The thickness of the washer and retaining seals are assumed to be negligible with no permeation through themselves.

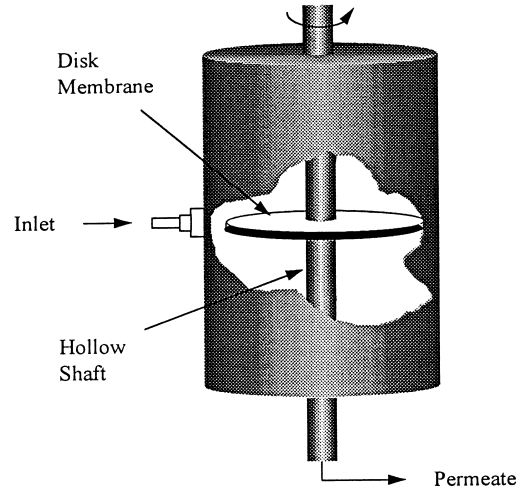

Fig. 1. Filtration unit.

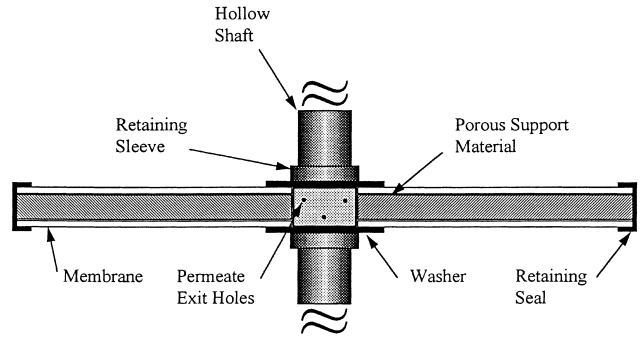

Fig. 2. Closer view of the rotating membrane disk.

2.2. Computational fluid dynamics

A commercial CFD package, FIDAP (Fluid Dynamics International, Evanston, IL), was used to model the hydrodynamics of this system. The fluid was assumed to be Newtonian, isothermal and incompressible. In laminar flow, the Navier–Stokes equations are solved by finite element method (FEM):

$$\nabla \cdot \boldsymbol{v} = 0 \tag{1}$$

$$\rho\left(\frac{\partial \boldsymbol{v}}{\partial t} + \boldsymbol{v} \cdot \nabla \boldsymbol{v}\right) = -\nabla p + \mu \nabla^2 \boldsymbol{v} + \rho \boldsymbol{f} \tag{2}$$

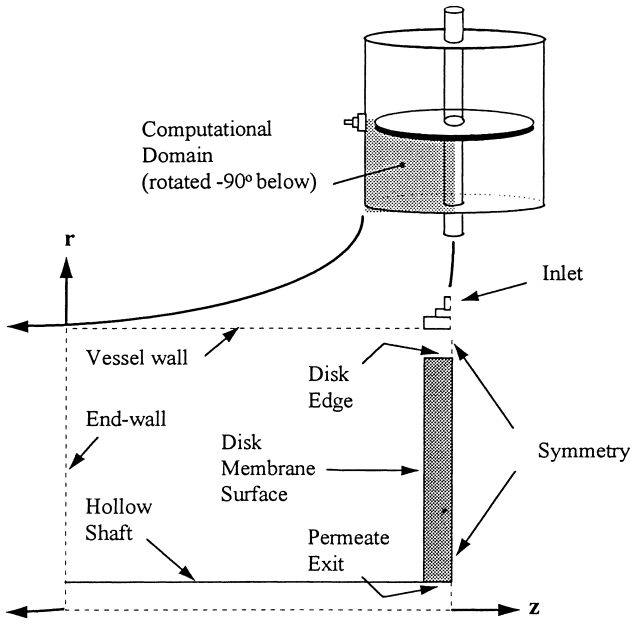

Fig. 3. Computational domain.

where ρ is the fluid density, $\boldsymbol{v}$ the Eulerian fluid velocity vector, p the pressure, μ the dynamic fluid viscosity and $\boldsymbol{f}$ the body force vector. The fluid flow equations (Eqs. (1) and (2)) is then solved only at nodal points on the FEM mesh. Inside each mesh element the velocity and pressure vectors are extrapolated.

Due to symmetry in cylindrical coordinates (r, θ, z), it suffices to model one-quadrant of the system in two-dimension (Fig. 3). The origin of the axial axis (z) is situated on the shaft while the origin of the radial axis (r) is placed at the end-wall. The reduced computational domain (i.e. the region of interest to be meshed) afforded by considering one-quarter of the entire system greatly facilitates in modeling fluid flow under turbulent conditions.

2.3. Turbulence model

The CFD tool used in this study allows for the use of two turbulence models, either the zero-equation model, based on the Prandtl mixing length, or the κ–ε model in which the turbulence field is characterized by the turbulent kinetic energy (κ) and the viscous dissipation rate of turbulent kinetic energy (ε). The κ–ε model was used in this investigation due to the presence of recirculating flows which should occur in our geometry. Previous studies [34,35] report that the κ–ε model appears to provide a more accurate description of experimental data obtained in such systems.

2.4. Permeation

The CFD tool can also accommodate numerous representations of flow in porous media. For a Newtonian, isothermal and incompressible fluid, flow through a porous medium can be described using the Forchheimer–Brinkman model:

$$\frac{\rho}{\phi}\frac{\partial \boldsymbol{v}}{\partial t} + \left[\frac{\mu}{L_\mathrm{p}} + \frac{\rho c}{\sqrt{L_\mathrm{p}}}||\boldsymbol{v}||^n\right]\boldsymbol{v} = -\nabla p + \mu\nabla^2\boldsymbol{v} + \rho\boldsymbol{f} \tag{3}$$

where ϕ is the medium porosity, c and n the constants which depend on the porous medium, L_p the porous medium permeability and $||\boldsymbol{v}||$ the magnitude of the velocity. Eq. (3) is similar to Eq. (2) except for the convection term which is replaced by the Darcy–Forchheimer term in brackets. Typically, the Forchheimer's term (second term within brackets) and the viscous flow term (second term of the right hand equation) can be neglected; in which case Eq. (3) becomes the expression of Darcy's law under conditions of steady flow and no body forces.

2.5. Assumptions and boundary conditions

Changes in global membrane permeability overtime due to the membrane fouling are not considered in this work. Thus, steady state solutions are calculated assuming a constant membrane permeability. No-slip boundary conditions are set at all solid wall boundaries (end-wall, vessel wall, non-porous disk surface, rotating shaft). The azimuthal velocity on the disk and shaft surface is set according to the equation:

$$v_\theta = r\omega \tag{4}$$

where r is the radial position. The axial and azimuthal inlet velocity are set at zero while a constant radial velocity is assumed. The axial outlet velocity is fixed at zero. The axial symmetry velocity is assumed to be equal to zero (see Fig. 3 for symmetry definition). The κ–ε boundary conditions are set at zero for the porous media and for the inlet and outlet since the flow at these locations is assumed to be laminar; while the value of turbulent kinetic energy (κ) and viscous dissipation rate of turbulent kinetic energy (ε) are set respectively, to $2.5 \times 10^3\ \mathrm{m^2\ s^{-2}}$ and $1.5 \times 10^6\ \mathrm{m^2\ s^{-3}}$ within the vessel.

2.6. Simulations

The global transmembrane pressure is defined as the difference between the inlet pressure and the permeate exit pressure (Fig. 3). The local transmembrane pressure is defined as the difference between the pressure at a given radial location on the feed side of the membrane and that on the permeate side at the same radial location. Since the simulation returns the pressure at each node, the local transmembrane pressure is actually calculated by the difference in pressure between two nodes having the same radial coordinate but situated at the feed and permeate membrane surfaces. Knowing the local transmembrane pressure for several radial positions (nodes), one can evaluate the dimensionless cumulative flow rate (Q^*) as the flow rate through the membrane from the washer tip to a radial

distance 'r' over the overall throughput flow rate (Q_0):

$$Q^*(r) = \frac{\int_{r_w}^{r} 2\pi(L_p/\mu e) r P_{tm,l}(r) dr}{Q_0} \quad (5)$$

where r_w is the radial position of the washer tip, e the membrane thickness and $P_{tm,l}$ the local transmembrane pressure. For convenience, one defines also a dimensionless radial position (R^*) and a dimensionless axial position (Z^*) as:

$$R^* = \frac{(r - r_w)}{(r_s - r_w)} \text{ for } r_w \leq r \leq r_s \quad (6)$$

$$Z^* = \frac{z}{s} \quad (7)$$

where r_s is the radial position of the retaining seal, z the axial position and s the clearance between the rotating disk and end-wall. Then the useful membrane area is characterized by R^* varying in the range from 0 to 1.

The code used in this study has been validated by Engler [11] by comparing the experimental global transmembrane pressure and the global transmembrane pressure returned by the simulation to achieve a specific flux. The discrepancy was found to be less than 7% so the code can be considered accurate enough to be used as a design tool.

Knowledge of the global and local transmembrane pressures is important in designing these membrane filters. The former is related to the energy consumption while the latter gives substantial information about the membrane performance. From each simulation, the dimensionless cumulative flow rate, the global and local transmembrane pressures are calculated and their variations with respect to system parameters are evaluated with the aim of improving filter design. Baseline values (Fig. 4) and ranges (see Table 1) for parameters in these simulations were selected to correspond to those anticipated in laboratory and full scale microfiltration units.

Table 1
Summary of parameter ranges

Parameter	Range
Inlet velocity (cm s^{-1})	0.027–0.063
Flow rate (l h^{-1})	1.45–3.40
Flux (l h^{-1} m^2)	150–350
Gap1 (cm)	0.2–1.6
Washer (cm)	0.4–2.0
Membrane permeability (cm^2)	0.5×10^{-12}–12.5×10^{-12}
Membrane resistance (m^{-1})	8×10^{10}–2×10^{12}
Support permeability (cm^2)	8.18×10^{-10}–8.18×10^{-6}
Support resistance (m^{-1})	4.28×10^{6}–4.28×10^{10}
Gap2 (cm)	0.34–7.14
Support thickness (cm)	0.15–0.55
Rotational speed (rpm)	0–1500

3. Results and discussion

3.1. Study of standard case: Effect of rotational speed

Variations in the pressure on the feed and permeate sides of the membrane were calculated with respect to the dimensionless radial position for different rotational speeds (Fig. 5). The feed side pressure remains relatively constant since the flow is evenly distributed thereby leading to very little pressure drop. However, in the support material, the flow rate increases from the disk tip to the permeate exit

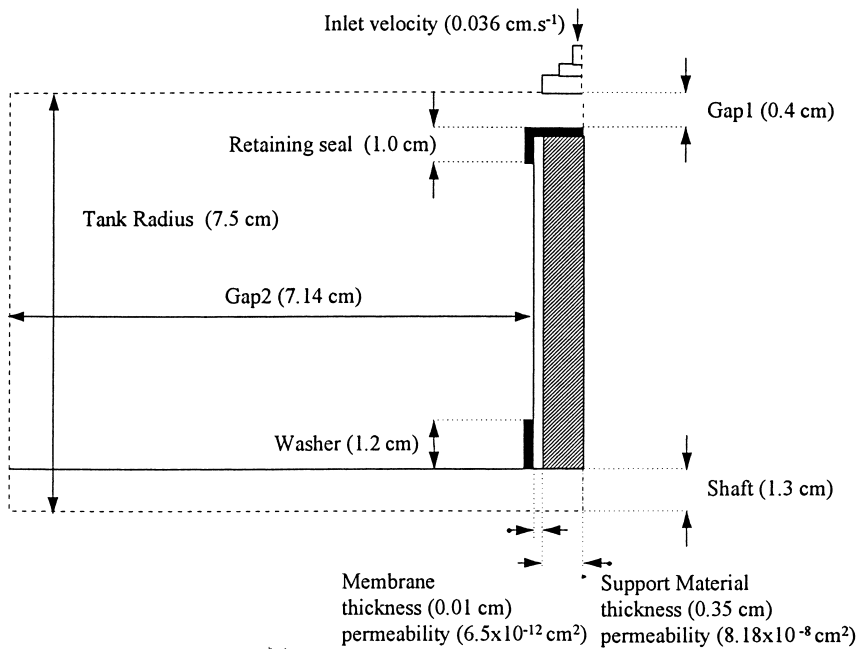

Fig. 4. Standard dimensions and parameters.

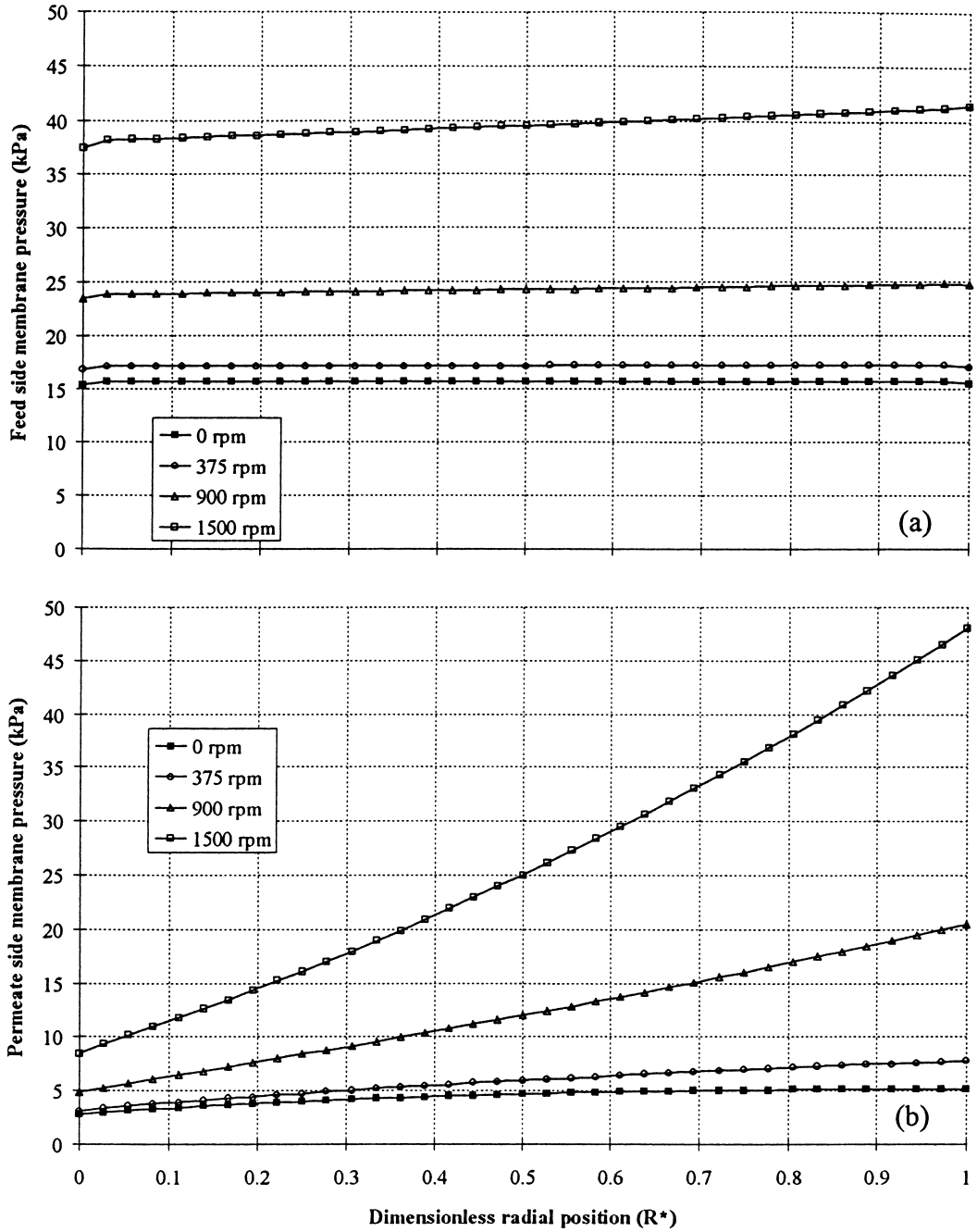

Fig. 5. Variations of feed (a) and permeate (b) side pressure as a function of radial position. Other parameters are at their 'standard' values.

with a concurrent pressure loss. Therefore, the local permeate pressure increases as the radial position increases. Also, the higher the rotational speed, the higher are the feed and permeate side pressures.

The permeate side pressure can be considered to result from a balance between pressure loss and centrifugal force effects. The centrifugal force acting on the fluid inside the support due to the disk rotation is proportional to the square of the rotational speed:

$$f_v = \rho r \omega^2 \quad (8)$$

Therefore there should be rotational speeds for which the centrifugal force effects are higher than the pressure loss effects of the porous support resulting in a local permeate pressure which is higher than the feed side pressure.

Due to the increase in permeate side pressure, the local transmembrane pressure decreases with increasing radial position (Fig. 6(a)). Therefore, the portions of the membrane closest to the shaft produce a higher increment in flow per unit of membrane area due to the higher permeate flux. This is illustrated by the variation of the dimensionless

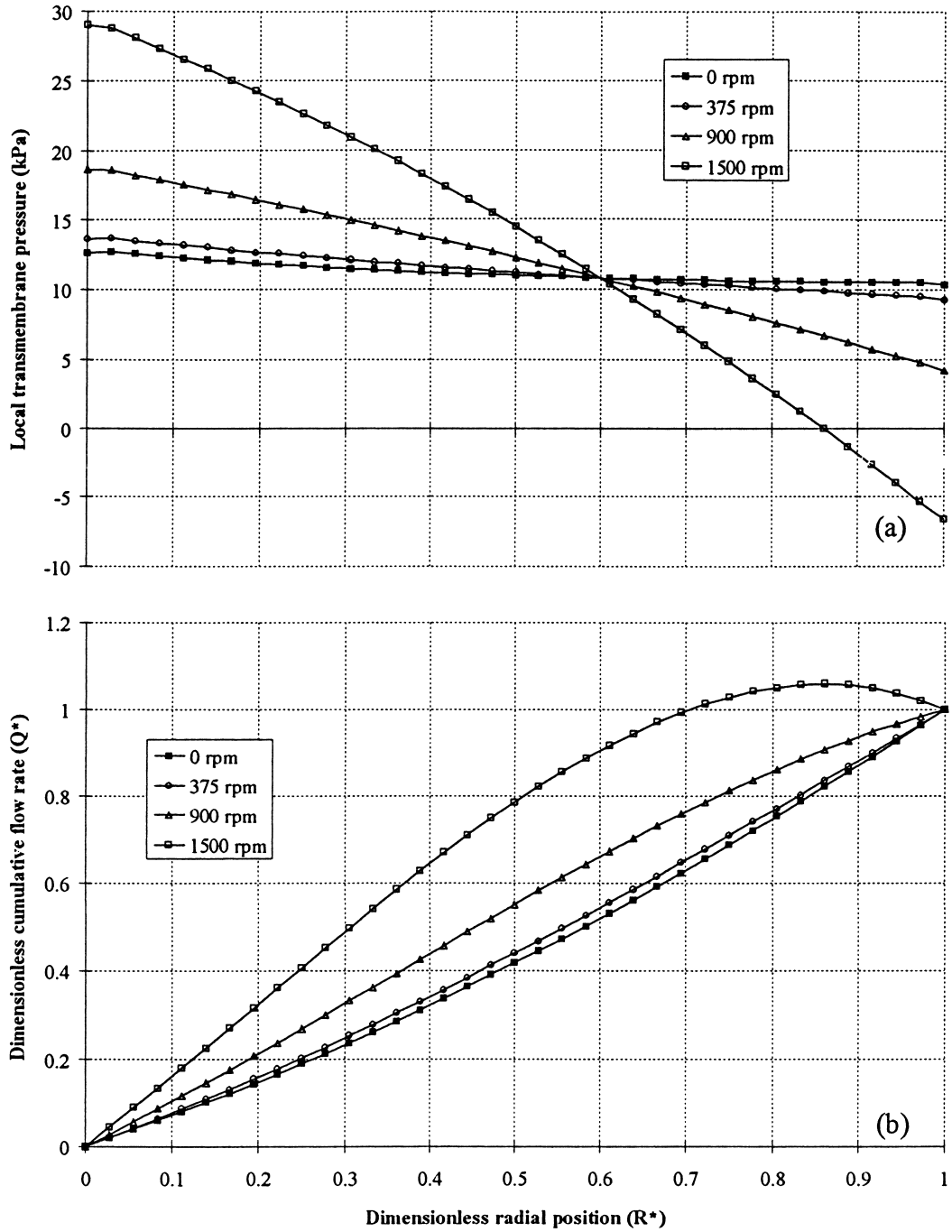

Fig. 6. Variations of local transmembrane pressure (a) and dimensionless cumulative flow rate (b) as a function of radial position. Other parameters are at their 'standard' values.

cumulative flow rate with the dimensionless radial position (Fig. 6(b)). For high rotational speeds, as a result of a higher permeate side pressure, the local transmembrane pressure exhibits some negative values and the dimensionless cumulative flow rate passes through a maximum. This means that a portion of the membrane is submitted to a reversed flow with some of the permeate returning to the feed compartment. In addition to reducing the effectiveness of installed membrane area, this 'back pressure' phenomenon might also damage the membrane over time since forces acting in an opposite direction could potentially tear the membrane from its support.

Higher rotational speeds produce higher global transmembrane pressures (Fig. 7). These higher global transmembrane pressures correspond to a higher energy consumption per unit of permeate since in all cases the total flow rate is constant.

Consistent with Eq. (4), the azimuthal velocity varies linearly with the radial position and the slope of the curve is equal to the rotational speed (Fig. 8(c)). The axial velocity

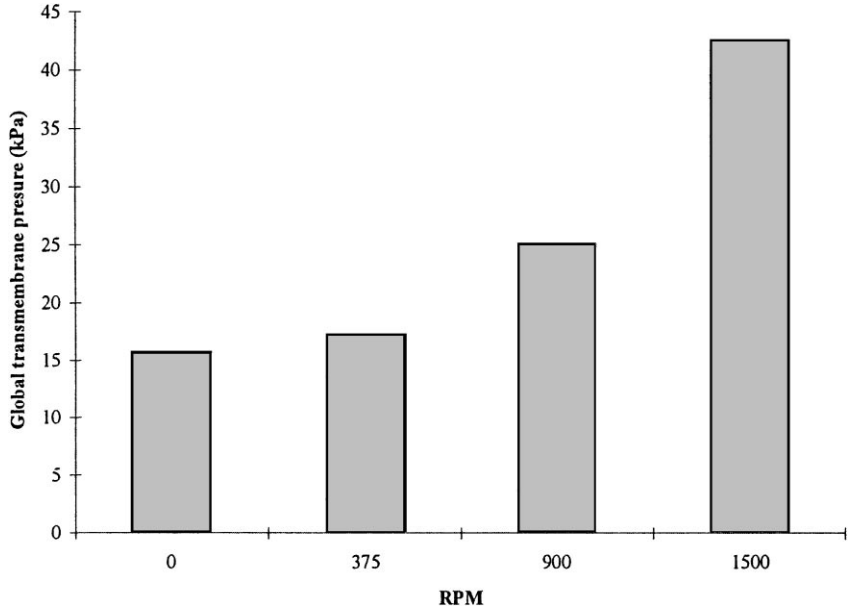

Fig. 7. Variations of the global transmembrane pressure as a function of rotational speed. Other parameters are at their 'standard' values.

(i.e. velocity through the membrane) exhibits the same variation as local transmembrane pressure (Fig. 8(b)) since they are linked by the permeability model (Eq. (3)) which, under simplifying assumptions, reduces to Darcy's law. Thus, the permeation velocity is higher at radial positions near the shaft where local transmembrane pressure is greater and smaller or negative for more distant radial positions. Irregularities at extreme values of radial distance (near the shaft and the membrane tip) are numerical artifacts that arise from the no-slip condition imposed to the washer and retaining seal. Axial velocity was set to zero at $R^* = 0$ and 1 which induces the nearest node velocity to be higher or smaller at the tip to keep the permeate flux in agreement with the local transmembrane pressure (Fig. 6(a)). For no rotation, the radial velocity remains equal to zero and no slip occurs at the membrane surface (Fig. 8(a)). As the disk rotation increases, the fluid starts to slip. Although the slip velocity increases with both radial position and speed of rotation, it remains small in comparison with the axial velocity.

Fig. 9 gives the axial variations of the velocity vector at the radial position 4.3 cm (middle of the membrane). From the azimuthal variation, one deduces that we are in the regime IV as defined by Daily and Nece [28] where the boundary layers on the end-wall and membrane disk are not merged. Thus, bulk fluid rotates at a smaller rotational speed than that in the disk boundary layer. Note that near the membrane disk, the azimuthal velocity drops slightly and then increases rapidly to reach the disk rotational speed. The slight drop is due to a radial movement of the fluid (Fig. 9(a)). The axial variation reflects fluid which is sucked up to the membrane surface compensating for the radial flow of fluid along the membrane. From the variation of the radial velocity, one can see that the fluid moves radially to the disk tip along the membrane surface (positive velocity for the highest dimensionless axial position) and returns radially to the shaft along the end-wall surface (negative velocity for the smallest dimensionless axial position). By comparison with this overall circulation, the bulk fluid moves very little.

The effect of disk rotation on the flow pattern is illustrated clearly on streamline contour plots representing stationary and rotating membrane disks (Figs. 10 and 11). Without rotation, streamlines in the inlet region bend around the retaining seal. As rotational speed increases, a dead-zone appears in which the fluid seems to circulate perpetually.

Disk rotation induces a higher shear stress on the membrane surface and is likely to reduce fouling. Subsequent results will be displayed only for a rotational speed of 1500 rpm at which speed fouling has been observed experimentally to be greatly reduced [11].

3.2. Effect of inlet velocity (filtration flux)

The local transmembrane pressure increases as the permeate flux (or equivalently the inlet velocity) increases (Fig. 12(a)). Since the centrifugal force depends only on the rotational speed and not on the inlet velocity, there is a value of permeate flux for which the effect of the 'back pressure' is overwhelmed. This effect can also be expressed as a minimum global transmembrane pressure required to overcome the rotationally induced 'back pressure' before permeation can occur (Fig. 12(b)). The global transmembrane pressure varies linearly with respect to the inlet velocity consistent with Darcy's law. The intercept indicates the value of the threshold 'back pressure' which must be overcomed to begin filtration. The higher the rotational speed the greater is this threshold 'back pressure'. Rotational speeds

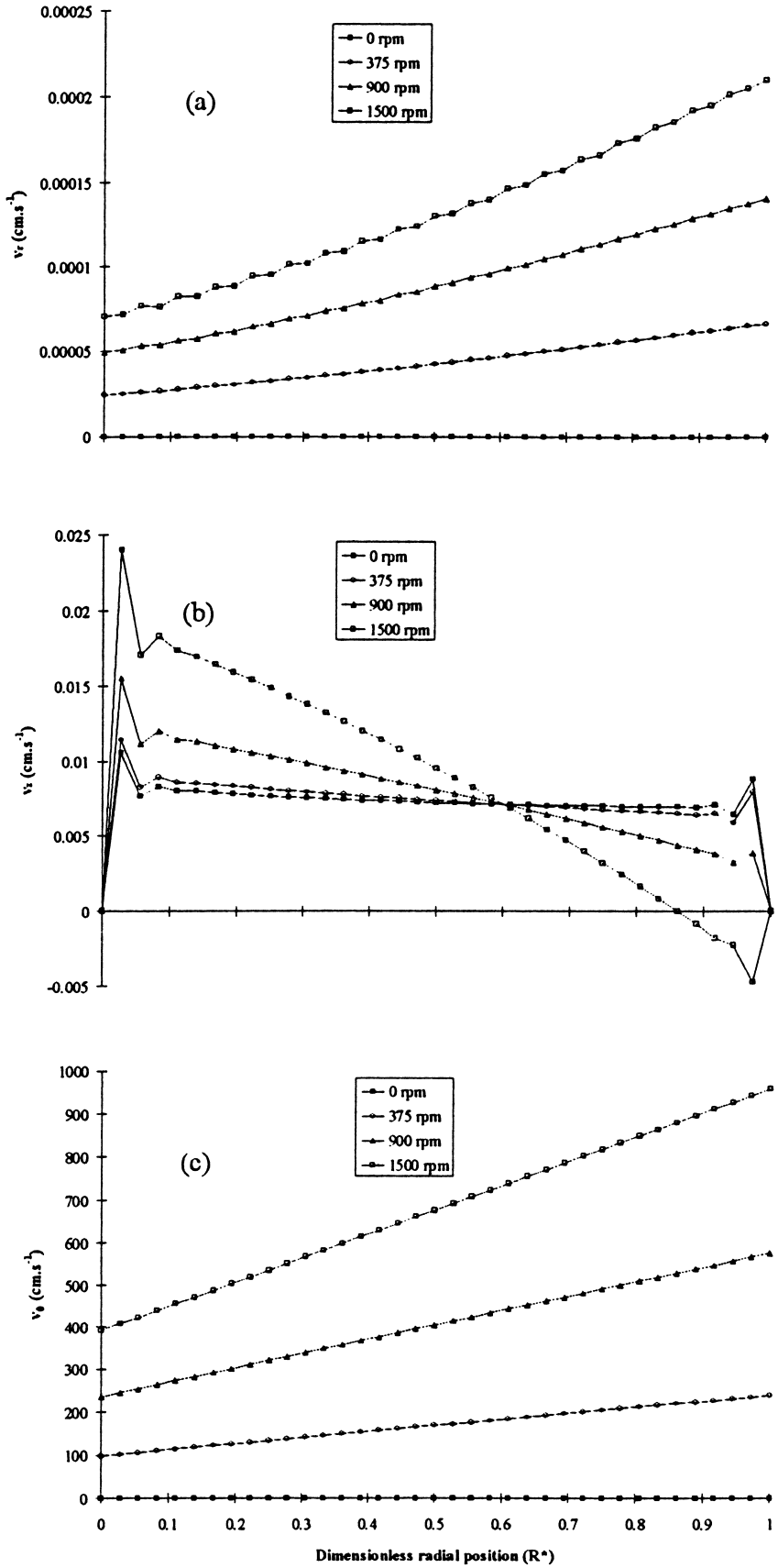

Fig. 8. Variations of the radial (a), axial (b) and azimuthal (c) velocity as a function of radial position ($z = 7.14$ cm). Other parameters are at their 'standard' values.

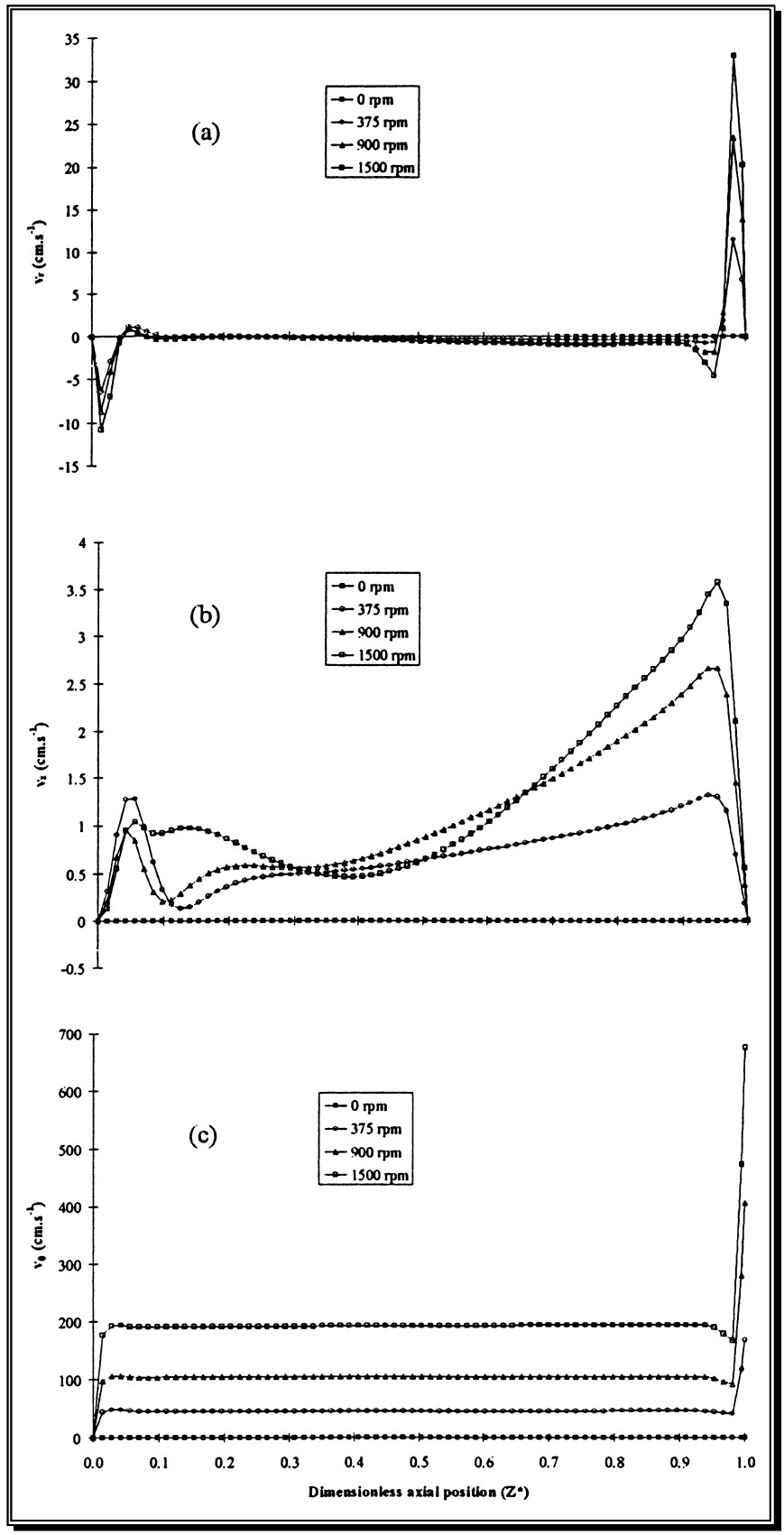

Fig. 9. Variations of the radial (a), axial (b) and azimuthal (c) velocity as a function of axial position ($r = 4.3$ cm). Other parameters are at their 'standard' values.

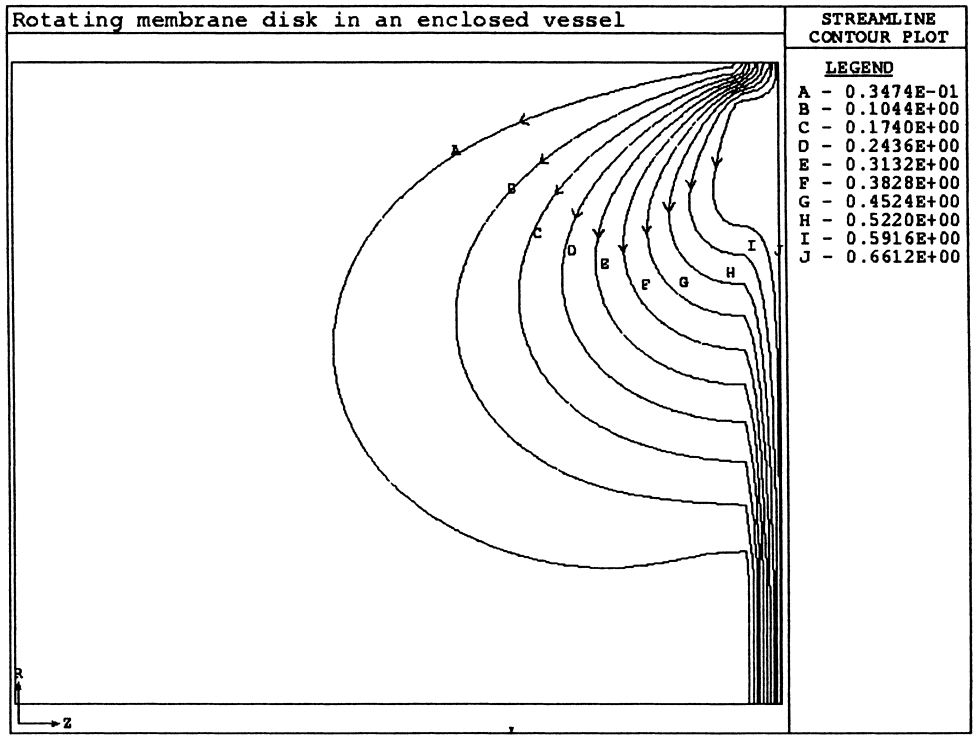

Fig. 10. Streamline contour plot and the subsequent values of the stream function for a rotational speed of 0 rpm. Other parameters are at their 'standard' values.

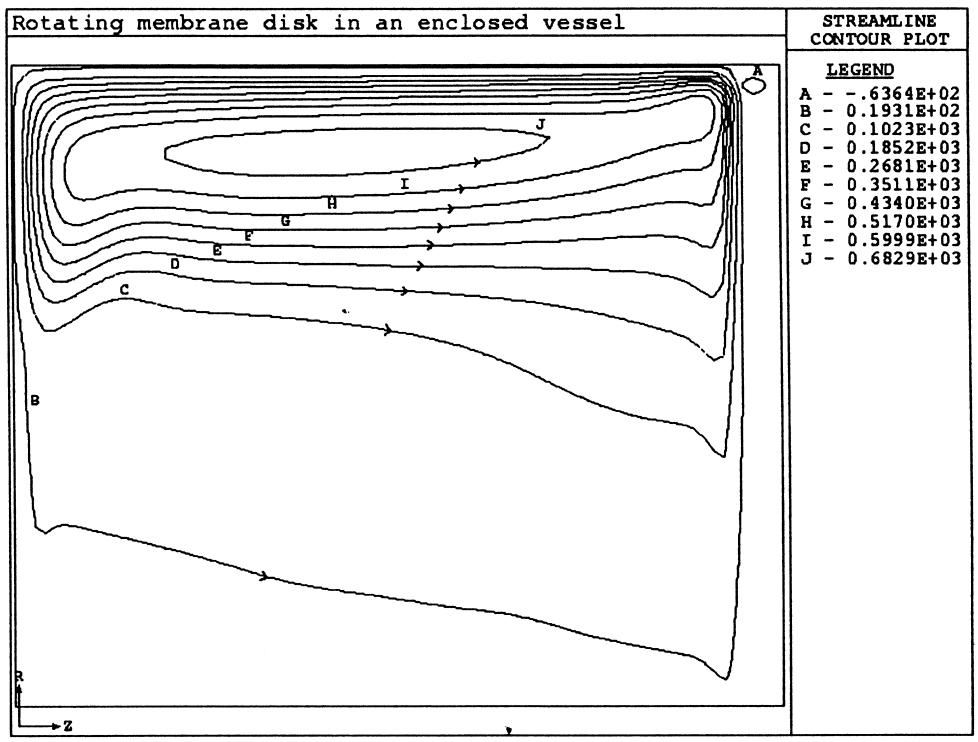

Fig. 11. Streamline contour plot and the subsequent values of the stream function for a rotational speed of 1500 rpm. Other parameters are at their 'standard' values.

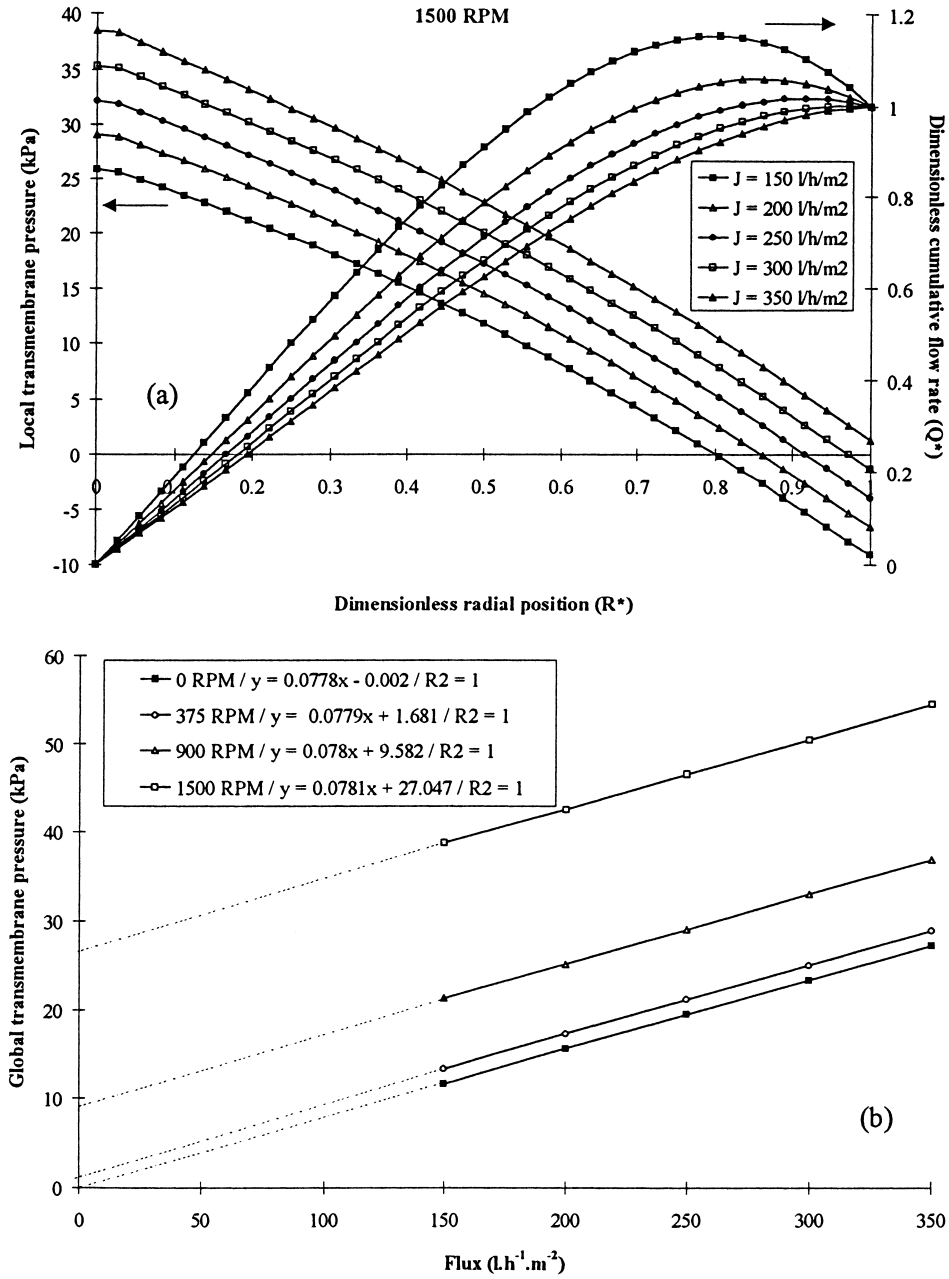

Fig. 12. Effect of permeate flux (J) on local transmembrane pressure and dimensionless cumulative flow rate (a) and on the global transmembrane pressure (b). Other parameters are at their 'standard' values.

of 375, 900 and 1500 rpm introduced calculated threshold 'back pressure' values of 1.7, 9.6 and 27 kPa, respectively.

3.3. *Effect of disk tip to vessel wall gap, retaining seal and washer lengths*

Variations in the local transmembrane pressure and dimensionless cumulative flow rate as a function of the dimensionless radial position for different values of the distance between the membrane disk tip and the vessel wall (Gap1) are rather significant (Fig. 13). High values of Gap1 correspond to conditions of small disk diameters. Smaller values of Gap1 (larger disk diameter) increase the 'back pressure' as permeate side pressure increases due to an increase in the centrifugal force. Indeed, according to Eq. (8), this force depends on the radial position (r). Smaller values of Gap1 correspond to larger radii to the membrane tip and hence the effect of the 'back pressure' is more important. Thus, there is a trade-off between obtaining higher values of the shear stress and reduced fouling with increasing disk diameter and rotational speed versus decreased membrane performance due to 'back pressure'. Therefore, to achieve a given flow rate at a given rotational speed, there is an optimal value of the disk diameter

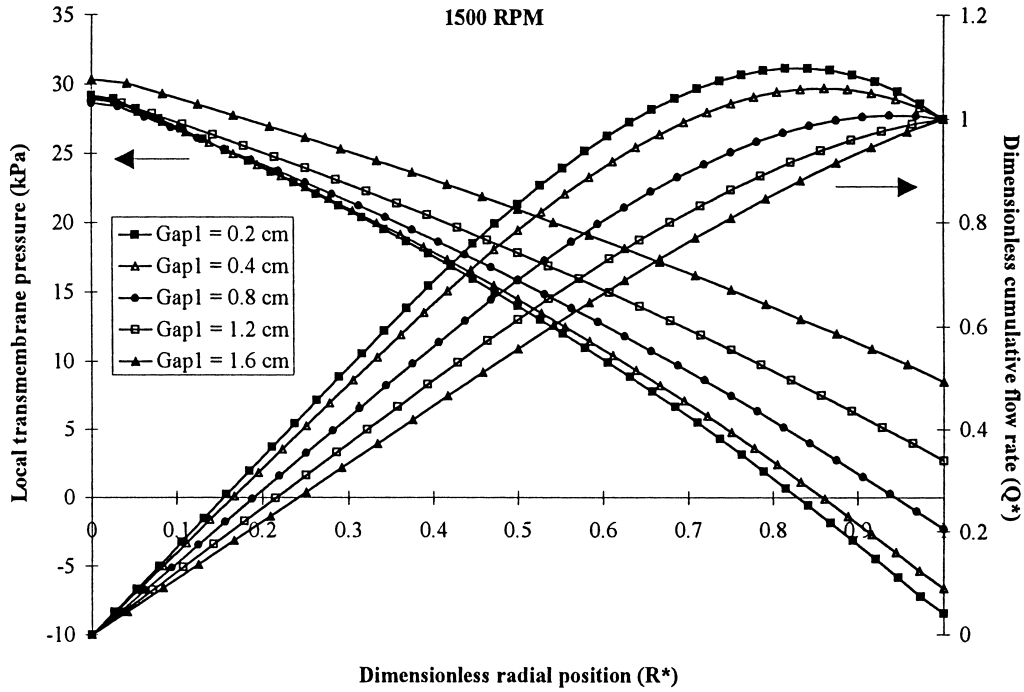

Fig. 13. Effect of the distance between disk tip and vessel (Gap1) on local transmembrane pressure and dimensionless cumulative flow rate. Other parameters are at their 'standard' values.

corresponding to a zero 'back pressure'. Due to an increase in the membrane filtering area, the global transmembrane pressure decreases when Gap1 is then decreased.

Retaining seal length has a similar effect to Gap1. Large values for the retaining seal length also roughly correspond to simulations with a smaller disk. Decreasing either will result in an increase in the 'back pressure' for the same reasons explained above. Hence, there is also an optimal value of the retaining seal length.

The effect of washer length is quite different (Fig. 14). The larger the washer, the smaller is the 'back pressure'. Due to the reduction in the membrane filtering area, the feed side pressure increases more than the permeate side pressure. The latter pressure increases primarily due to pressure loss effects rather than by centrifugal force effects. In fact, the centrifugal force changes little since there is little variation in the radial position of the membrane tip. Pressure loss increases as more fluid flows into a smaller region and a higher global transmembrane pressure is produced.

3.4. Effect of membrane and support permeabilities

Membrane permeability has a strong influence on the 'back pressure' effect; a higher permeability results in a higher 'back pressure' (Fig. 15). As permeability increases, less pressure is required to produce the same flow through the membrane. Hence, the permeate side pressure may exceed the feed pressure resulting in the presence of 'back pressure'. However, it is likely that high membrane permeabilities will be exploited to operate at higher flow rates or smaller membrane areas. There is an optimal radial position of membrane tip (disk diameter) defined as the diameter at which 'back pressure' is equal to zero (Fig. 16). Disk diameters larger than this optimum are likely to provide membrane area which is under-utilized or ineffective.

The support permeability is typically much greater than the membrane permeability and the resistance to permeation is due primarily to the membrane. Therefore, system performances and choice of disk diameter are less sensitive to the permeability of the support than they are to the permeability of the membrane (Fig. 17). As the support permeability approaches that of the membrane, the sensitivity of the global and local transmembrane pressures and dimensionless cumulative flow rate to future reductions in permeability or changes in disk radius are similar to those for the membrane alone.

3.5. Effect of support thickness and the distance between membrane surface and end-wall

Over the range of support thickness evaluated (Fig. 18), a trend toward decreased 'back pressure' with increased support thickness is predicted. This can be readily explained if one considers the support as a pipe in which flows the permeate. The thicker the pipe, the smaller is the pressure loss and thus the permeate side pressure.

The clearance between the membrane disk and end-wall (Gap2) has a small effect (Fig. 19). Even for the smallest clearance (0.34 cm), the boundary layers are separated. A small gap width between membrane disk and adjacent baffles is desirable on a full scale unit from the standpoint

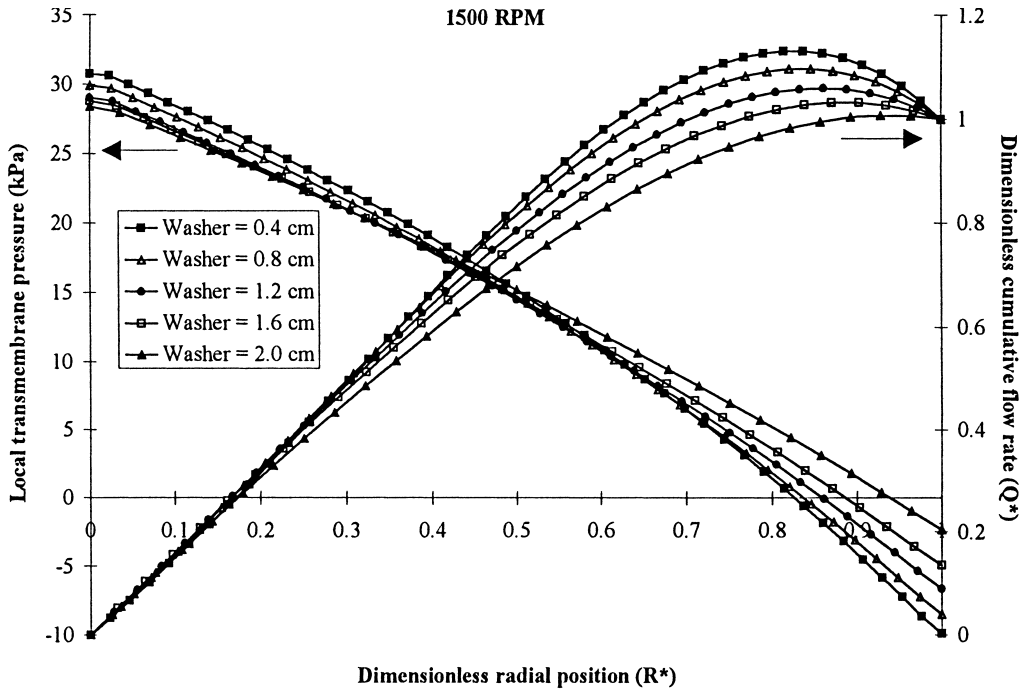

Fig. 14. Effect of washer length on local transmembrane pressure and dimensionless cumulative flow rate. Other parameters are at their 'standard' values.

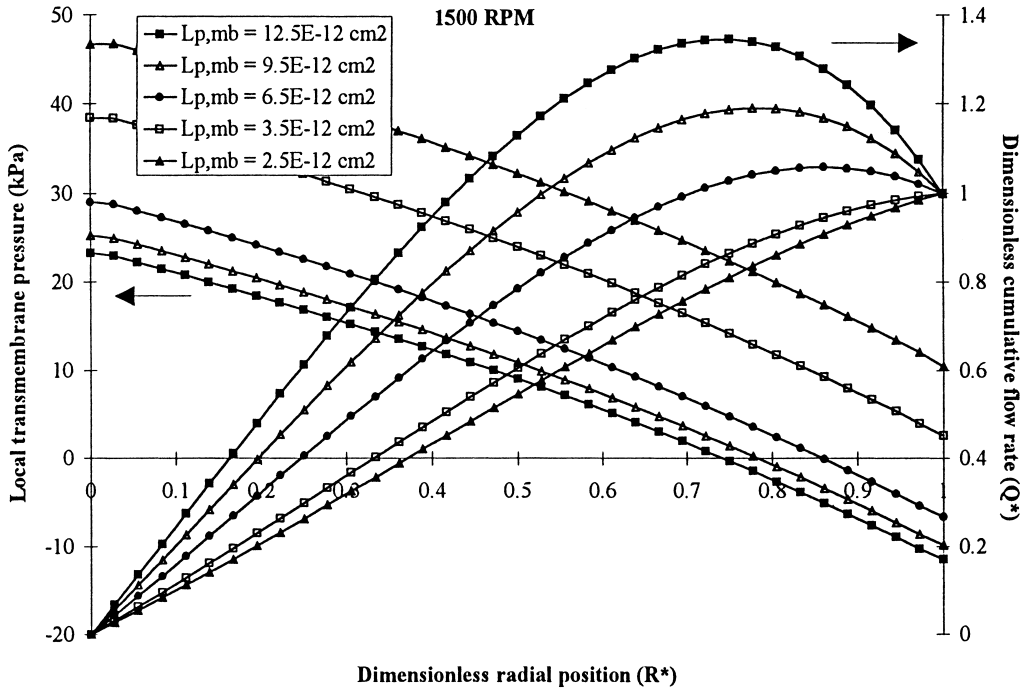

Fig. 15. Effect of membrane permeability ($L_{p,mb}$) on local transmembrane pressure and dimensionless cumulative flow rate. Other parameters are at their 'standard' values.

of packing density. However, a small gap width will also entail greater energy consumption as feed solid concentration and the resultant viscosity increase. The clearance selected for design should therefore reflect a balance between packing density, power consumption and particle concentration considerations.

4. Conclusions

The centrifugal force acting on fluid permeating into a rotating membrane disk may result in a local permeate side pressure that is higher than the feed side pressure at high enough rotational speeds and radial distances from the shaft.

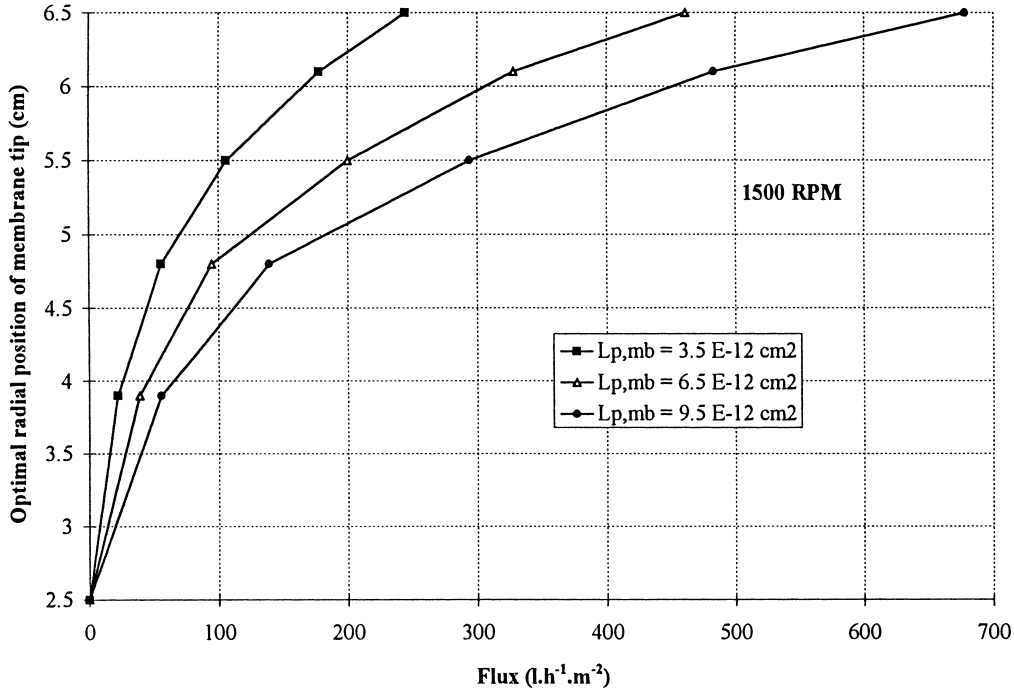

Fig. 16. Effect of membrane permeability ($L_{p,mb}$) on the optimal radial position of membrane tip for a rotational speed of 1500 rpm. Other parameters are at their 'standard' values.

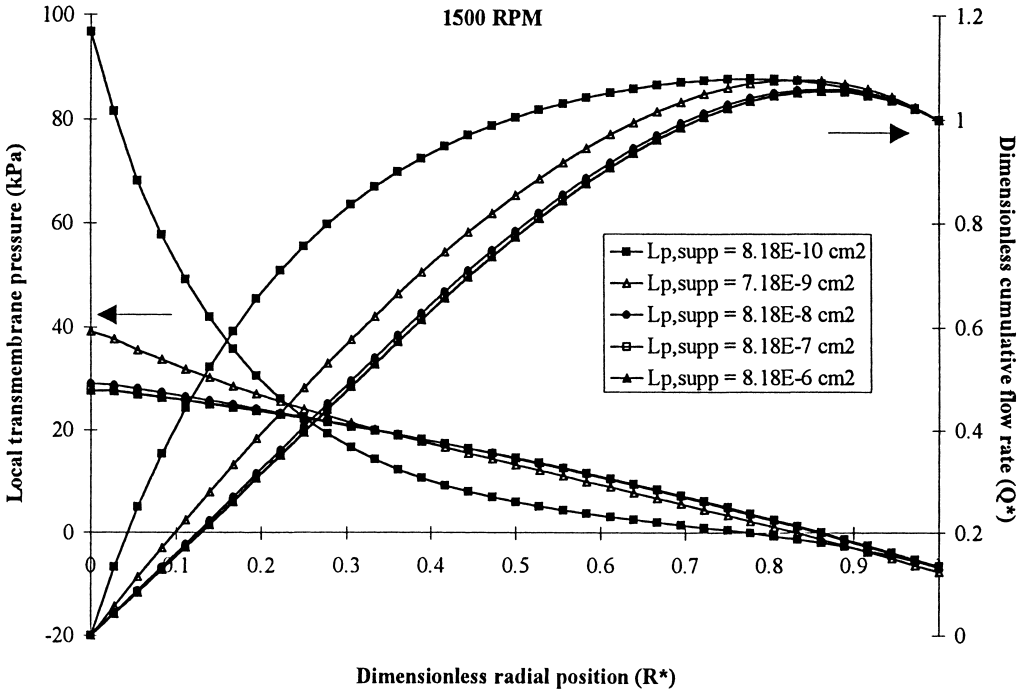

Fig. 17. Effect of support permeability ($L_{p,supp}$) on local transmembrane pressure and dimensionless cumulative flow rate. Other parameters are at their 'standard' values.

A portion of the membrane is then characterized by a negative local transmembrane pressure and, as a resultant, permeate flows in a reverse direction back across the membrane. The design and operating conditions of such systems should minimize this 'back pressure' phenomenon which reduces the effectiveness of the membrane area and may also damage the membrane. This can be achieved by either increasing the flow rate (within the limits of membrane and support permeabilities), decreasing the disk diameter or increasing the washer and retaining seal lengths. The disk diameter is likely to be key in scaling up such systems. The membrane and support permeabilities have a

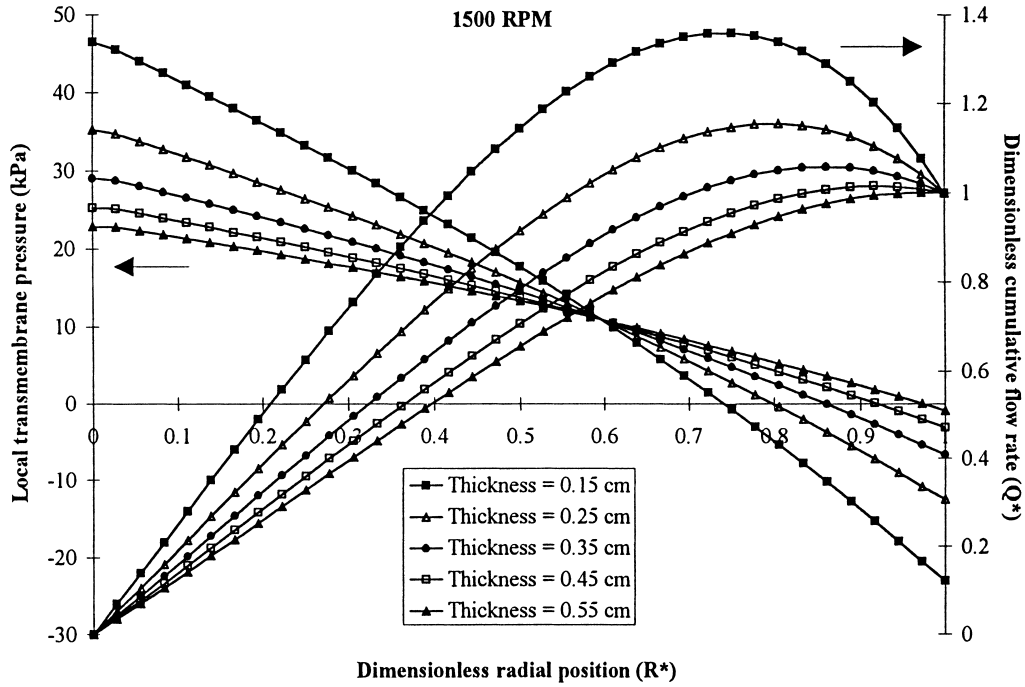

Fig. 18. Effect of support thickness on local transmembrane pressure and dimensionless cumulative flow rate. Other parameters are at their 'standard' values.

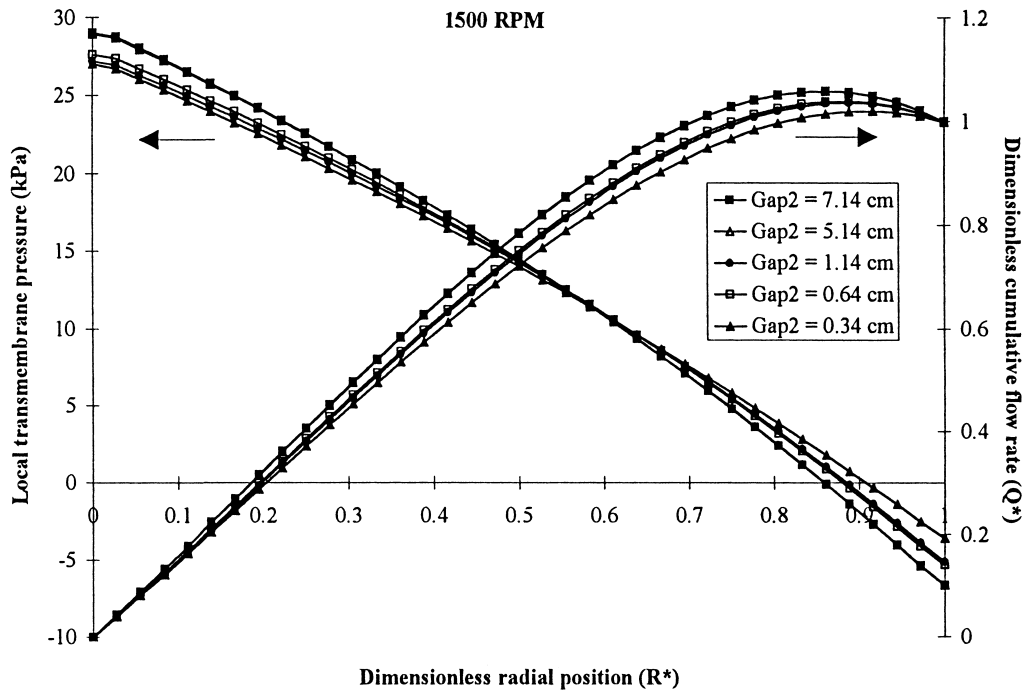

Fig. 19. Effect of the clearance between the membrane disk and end-wall (Gap2) on local transmembrane pressure and dimensionless cumulative flow. Other parameters are at their 'standard' values.

strong influence on the 'back pressure'. Higher permeabilities require smaller disk diameters. The effects of clearance between the membrane disk and end-wall on the fluid mechanics of a clean membrane appear to be small. For the smallest clearance studied, the boundary layers on the membrane disk and end-wall surfaces are still separated. Thus, high packing densities should not compromise performance within the limits imposed by the feed suspension viscosity and the desirability of a thicker support for reduced pressure loss.

5. Nomenclature

Latin notation

c	constant (−), Eq. (3)
e	membrane thickness (m)
f	body force (N kg^{-1})
f_v	volumetric force (N m^{-3})
L_p	permeability coefficient (m^2)
n	constant (−), Eq. (3)
p	pressure (Pa)
$P_{tm,l}$	local transmembrane pressure (Pa)
Q^*	dimensionless cumulative flow rate (−), Eq. (5)
Q_0	overall throughput flow rate (m^3 s^{-1})
R^*	dimensionless radial position (−), Eq. (5)
R	disk radius (m)
r	radial position (m)
Re	Reynolds number (−)
r_s	radial position of retaining seal (m)
r_w	radial position of washer tip (m)
s	clearance between the rotating disk and end-wall (m)
t	time (s)
v	velocity (m s^{-1})
Z^*	dimensionless axial position (−), Eq. (7)
z	axial position (m)

Greek symbol

θ	azimuthal position (rad)
μ	dynamic fluid viscosity (Pa s)
ρ	fluid density (kg m^{-3})
ϕ	medium porosity (−)
ω	rotational speed (s^{-1})
κ	turbulent kinetic energy (m^2 s^{-2})
ε	viscous dissipation rate of turbulent kinetic energy (m^2 s^{-3})
ν	kinematic viscosity (m^2 s^{-1})

Subscript

mb	relative to the membrane
supp	relative to the support material
θ	azimuthal component
r	radial component
z	axial component

Acknowledgements

The authors wish to express their gratitude to Suez – Lyonnaise des Eaux for financial support for this work.

References

[1] H. Strathmann, Economic assessment of membrane processes, Proc. EEC-Brazil Workshop on Membrane Separation Processes, Rio de Janeiro, Brazil, 1992.
[2] J. Mallevialle, P.E. Odendaal, M.R. Wiesner, The emergence of membranes in water and wastewater treatment, in: J. Mallevialle, P.E. Odendaal, M.R. Wiesner (Eds.), Water Treatment: Membrane Processes, McGraw-Hill, New York, 1996.
[3] T. Murase, C. Pradistsuwana, E. Iritani, K. Kano, Dynamic microfiltration of dilute slurries with a rotating ceramic membrane, J. Membr. Sci. 62 (1991) 187–199.
[4] N. Ohkuma, T. Shinoda, T. Aoi, Y. Okaniwa, Y. Magara, Performance of rotating disk modules in a collected human excreta treatment plant, Wat. Sci. Tech. 30(4) (1994) 141–149.
[5] J.Y. Park, C.K. Choi, J.J. Kim, A study on dynamic separation of silica slurry using a rotating membrane filter. 1. Experiments and filtrate fluxes, J. Membr. Sci. 97 (1994) 263–273.
[6] B. Riesmeier, K.H. Kroner, M.-R. Kula, Harvest of microbial suspensions by microfiltration, Desalination 77 (1990) 219–233.
[7] K. Nakano, M. Matsumura, H. Kataoka, Application of a rotating ceramic membrane to dense cell culture, J. Ferment. Bioeng. 76(1) (1993) 49–54.
[8] C.S. Parnham, R.H. Davis, Protein recovery from cell debris using rotating and tangential crossflow microfiltration, Biotechnol. Bioeng. 47 (1995) 155–164.
[9] U. Frenander, A.-S. Jönsson, Cell harvesting by cross-flow microfiltration using a shear-enhanced module, Biotechnol. Bioeng. 52 (1996) 397–403.
[10] J.A. Engler, M.R. Wiesner, C. Anselme, Treatment of PAC slurry using rotating disk membrane, in: Proc. 1995 Membrane technologie conference, Reno, vol. 1, 1995, pp. 747–758.
[11] J.A. Engler, Investigation of membrane filtration in a rotating disk geometry: Use of computational fluid dynamics and laboratory evaluation, Doctoral thesis, Rice University, Houston, 1997.
[12] J. Murkes, C.G. Carlson, High shear crossflow filtration, in: Crossflow Filtration: Theory and Practice, Wiley, Houston, 1988.
[13] K.H. Kroner, V. Nissinen, Dynamic filtration of microbial suspensions using an axially rotating filter, J. Membr. Sci. 36 (1988) 85–100.
[14] T. Murase, E. Iritani, P. Chidphong, K. Kano, K. Atsumi, M. Shirato, High-speed microfiltration using a rotating, cylindrical, ceramic membrane, Int. chem. Eng. 31(2) (1991) 370–377.
[15] U.B. Holeschovsky, C.L. Cooney, Quantitative description of ultrafiltration rotating filtration device, AIChE J. 37(8) (1991) 1219–1226.
[16] T. Murase, E. Iritani, P. Chidphong, K. Kano, Periodic dynamic filtration using a ceramic filter with a rotating cylinder, Int. chem. Eng. 32(2) (1992) 352–359.
[17] R.G. Holdich, G.M. Zhang, Crossflow microfiltration incorporting rotational fluid flow, Trans IChemE 70(A) (1992) 527–536.
[18] G. Belfort, J.M. Pimbley, A. Greiner, K.Y. Chung, Diagnosis of membrane fouling using a rotating annular filter. 1. Cell culture media, J. Membr. Sci. 77 (1993) 1–22.
[19] G. Belfort, P. Mikulasek, J.M. Pimbley, K.Y. Chung, Diagnosis of membrane fouling using a rotating annular filter. 2. Dilute particle suspensions of known particle size, J. Membr. Sci. 77 (1993) 23–29.
[20] P. Mikulasek, P. Dolecek, Use of a rotating filter to enhance ceramic membrane filtration performance of latex dispersions, Sep. Sci. Technol. 29(15) (1994) 1943–1956.
[21] P. Dolecek, P. Mikulasek, G. Belfort, The performance of a rotating filter. 1. Theoretical analysis of the flow in an annulus with a rotating inner porous wall, J. Membr. Sci. 99 (1995) 241–248.
[22] A.S. Jönsson, Influence of shear rate on the flux during ultrafiltration of colloidal substances, J. Membr. Sci. 79 (1993) 93–99.

[23] M.C. Aubert, M.P. Elluard, H. Barnier, Shear stress induced erosion of filtration cake studied by a flat rotating disk method. Determination of the critical shear stress erosion, J. Membr. Sci. 84 (1993) 229–240.
[24] K. Michel, V. Gruber, Experience with continuous pressure filtration in new disk-type filter, Chem. Ing. Tech. 34 (1970) 773–779.
[25] N. Scweigler, W. Stahl, High performance disc filter for dewatering mineral sluries, Filtr. Sep., Jan/Feb (1990) 38–41.
[26] S.S. Lee, A. Burt, G. Russotti, B. Buckland, Microfiltration of recombinant yeast cells using disk dynamic filtration system, Biotechnol. Bioeng. 48 (1995) 386–400.
[27] S.L. Soo, N.J. Princeton, Laminar flow over an unclosed rotating disk, Trans. ASME 80 (1958) 287–296.
[28] J.W. Daily, R.E. Nece, Chamber dimension effects on induced flow and frictional resistance of enclosed rotating disks, Trans. ASME: J. Basic Eng., March (1960) 217–232.
[29] Schlichting H., Boundary-Layer Theory, McGraw-Hill, New-York, 1968.
[30] L.O. Wilson, N.L. Schryer, Flow between a stationary and a rotating disk with suction, J. Fluid. Mech. 85(3) (1978) 479–496.
[31] A.Z. Szeri, S.J. Schneider, F. Labbe, Flow between rotating disks. I. Basic flow, J. Fluid. Mech. 134 (1983) 103–131.
[32] W.-M. Lu, C.-J. Chuang, Effect of permeation through stator on the hydrodynamics of a rotating disk dynamic filter, J. Chem. Eng. Jpn. 21(4) (1988) 238–374.
[33] L. Rudniak, S. Wronski, Laminar flow hydrodynamics of rotating dynamics filters, Chem. Eng. J. 58 (1995) 145–150.
[34] J.W. Chew, Computation of flow and heat transfer in rotating disc system, Theoretical Science Group, Rolls Royce, Derby, 1987.
[35] M. Williams, W.C. Chen, G. Bache, A. Eastland, Methodology of internal swirling flow systems with a rotating wall, J. Turbomachinery 113 (1991) 83–90.